Journal of Alloys and Compounds 505 (2010) 172–178

Contents lists available at ScienceDirect

Journal of Alloys and Compounds

journal homepage: www.elsevier.com/locate/jallcom

L-Histidine coated iron oxide nanoparticles: Synthesis, structural and conductivity characterization

B. Ünal[a], Z. Durmus[b], A. Baykal[b,*], H. Sözeri[c], M.S. Toprak[d], L. Alpsoy[e]

[a] Department of Physics, Fatih University, B. Cekmece, 34500 Istanbul, Turkey
[b] Department of Chemistry, Fatih University, B. Cekmece, 34500 Istanbul, Turkey
[c] TUBITAK-UME, National Metrology Institute, PO Box 54, 41470, Gebze-Kocaeli, Turkey
[d] Department of Functional Materials, Royal Institute of Technology, SE16440 Stockholm, Sweden
[e] Department of Biology, Fatih University, B. Cekmece, 34500 Istanbul, Turkey

ARTICLE INFO

Article history:
Received 5 February 2010
Accepted 5 June 2010
Available online 12 June 2010

Keywords:
L-Histidine
Magnetic nanoparticles
Surface modification
Magnetic property conductivity

ABSTRACT

L-Histidine capped iron oxide nanoparticles (HCIO) have been synthesized in one pot in the presence of L-histidine. The final product was analyzed for composition, microstructure, *ac–dc* conductivity performance as well as dielectric permittivity. Results revealed that magnetic nanoparticles are maghemite (or magnetite) and L-histidine is covalently bonded to the nanoparticle surface via carboxyl groups. Thermal analysis revealed that magnetic nanoparticles showed catalytic effect that caused an early degradation/decomposition of the L-histidine capping. Near spherical morphology was assessed by TEM and particle size calculated from TEM analysis and crystallite size calculated from XRD analysis reveal single crystalline nature of iron oxide NPs. Magnetic measurements reveal the superparamagnetic character of the nanoparticles, hence the nanocomposite. The *ac* conductivity showed a temperature-dependent behavior at low frequencies and temperature independent behavior at high frequencies which is an indication of ionic conductivity. The *dc* conductivity of the nanocomposites is found to obey the Arrhenius plot with activation energy of 0.934 eV. Analysis of electrical modulus and dielectric permittivity functions suggest that ionic and polymer segmental motions are strongly coupled in the nanocomposite.

1. Introduction

Transition metal oxides have been of scientific and technological interest for many decades due to their interesting optical, magnetic, electrical and catalytical properties. Among these, magnetite (Fe_3O_4) is a common magnetic iron oxide that has a cubic inverse spinel structure with fcc close packed oxygens and Fe cations occupying interstitial tetrahedral and octahedral sites [1]. Magnetite unit cell can be represented with the formula $(Fe_8^{3+})_A[Fe_{40/3}^{3+}Fe_{8/3}^{2+}]_BO_{32}$, where A and B indicates tetrahedral and octahedral positioning, respectively. The electrons can hop between Fe^{2+} and Fe^{3+} ions in the octahedral sites at room temperature, rendering magnetite an important class of half-metallic materials [2,3].

In clinical area, magnetic nanoparticles are used as delivery systems for drugs [4], in medical diagnosis [5], hyperthermia [6], and cell separation [7]. Most of these applications require chemically stable, well-dispersed and uniform size particles. For this reason, new technologies in synthesis and methods of analysis have been developed. One of the effective approaches for preventing particle agglomeration is to coat nanoparticles with polymers or other targeting agents, taking into account their biocompatibility. Among the chemicals which may be used towards achieving this aim, aminoacids are suitable because they play a very important role in the body [8]. Aminoacids are very desirable chemicals as ligands anchored with magnetic nanoparticles. Therapy with amino acid imbalance or with amino acids as a dose of nutrients has been widely used to treat cancer sufferers because some amino acids reduced tumor cells. Excess of amino acid, would lead to the tumor cell shrinking or even dying out [9–11].

The importance of histidine lies in the fact that the body uses it to manufacture histamine, and histamine is responsible for a wide range of physiological processes. In therapy, histidine has been claimed of being useful in decreasing blood pressure because of its vasodilatory effects. Also it is used as supplement in therapy of rheumatoid arthritis, and is, like many other aminoacids, important for growth and general tissue repair. The ability of histidine to act as an electron donor and, thereby, to neutralize singlet oxygen and the hydroxyl radical results in improved contractility and heart function during a heart attack or cardiologycal procedures such heart bypass, heart transplant, angioplasty [12].

In a recent worked we reported on the a spontaneous, single-step synthesis of magnetic nanoparticulate spheres using

* Corresponding author. Tel.: +90 212 866 33 00/2061; fax: +90 212 866 34 02.
E-mail address: hbaykal@fatih.edu.tr (A. Baykal).

0925-8388/$ – see front matter © 2010 Elsevier B.V. All rights reserved.
doi:10.1016/j.jallcom.2010.06.022

a combination of positively charged poly-L-lysine and negatively charged iron oxide nanoparticles [13]. In this study, we aim at a new synthesis route to prepare aminoacid modified iron oxide in one step. To our knowledge, only few studies about the capping of the aminoacids on the surface of the magnetic nanoparticles were realized [14,9]. This process may have potential applications to synthesize other aminoacid capped nanoparticle configurations, including essential aminoacids and some proteins coating. In addition, the synthesized aminoacid-coated magnetic nanoparticles might be applied to cell separation, diagnosis and targeted drug delivery for cancer therapy.

2. Experimental

2.1. Synthesis

All chemicals ($FeCl_3{\cdot}2H_2O$, $FeCl_2{\cdot}4H_2O$, L-histidine) were obtained from Merck and were used without further purification. To an aqueous solution of a mixture of Fe(III) and Fe(II) salts, L-histidine solution in the molar ratio 2Fe(III):1Fe(II):4 L-histidine was added and kept at a constant temperature of 40 °C for 15 min under vigorous stirring. Then a solution of ammonium hydroxide was added till the pH was raised to ~11 at which a black suspension was formed. This suspension was then refluxed at 80 °C for 6 h, under vigorous stirring and Ar gas. HCIO particles were separated from the aqueous solution by magnetic decantation washed with distilled water several times and then dried in an oven overnight.

2.2. Characterization

X-ray powder diffraction (XRD) analysis was conducted on a Huber JSODebyeflex 1001 Diffractometer operated at 40 kV and 35 mA using Cu Kα radiation.

Transmission electron microscopy (TEM) analysis was performed using a FEI Tecnai G2 Sphera microscope. A drop of diluted sample in alcohol was dripped on a TEM grid.

Fourier transform infrared (FT-IR) spectra were recorded in transmission mode with a PerkinElmer BX FT-IR infrared spectrometer. The powder samples were ground with KBr and compressed into a pellet. FT-IR spectra in the range 4000–400 cm^{-1} were recorded in order to investigate the nature of the chemical bonds formed.

The real (ε') and imaginary (ε'') parts of complex dielectric permittivity $\varepsilon^* [= \varepsilon'(\omega) + i\varepsilon''(\omega)]$ were measured with a Novocontrol dielectric-impedance analyzer. The dielectric data (ε', ε'') were collected during heating as a function of frequency. The films were sandwiched between gold blocking electrodes and the conductivities were measured in the frequency range 0.1 Hz to 1 MHz at 10 °C intervals. The temperature was controlled with a Novocontrol cryosystem, which is applicable between −100 and 250 °C.

VSM measurements were performed by using a Vibrating sample magnetometer (LDJ Electronics Inc., Model 9600). The magnetization measurements were carried out in an extenal field up to 15 kOe at room temperature.

The thermal stability was determined by thermogravimetric analysis (TGA, PerkinElmer Instruments model, STA 6000). The TGA thermograms were recorded for 5 mg of powder sample at a heating rate of 10 °C/min in the temperature range of 30–800 °C under nitrogen atmosphere.

3. Results and discussion

3.1. XRD analysis

Phase investigation of the crystallized product was performed by XRD and the diffraction pattern is presented in Fig. 1. The XRD pattern indicates that the product consists of magnetite, Fe_3O_4, and the diffraction peaks are broadened owing to very small crystallite size. All of the observed diffraction peaks are indexed by the cubic structure of Fe_3O_4 (JCPDS no. 19-629) revealing a high phase purity of magnetite. EDX analysis also confirmed this formula. The mean size of the crystallites was estimated from the diffraction pattern by line profile fitting method using the Eq. (1) given in Refs. [15,16]. The line profile, shown in Fig. 1 was fitted for observed six peaks with the following miller indices: (2 2 0), (3 1 1), (4 0 0), (4 2 2), (5 1 1), (4 4 0). The average crystallite size, D and σ, was obtained as 7 ± 1 nm as a result of this line profile fitting.

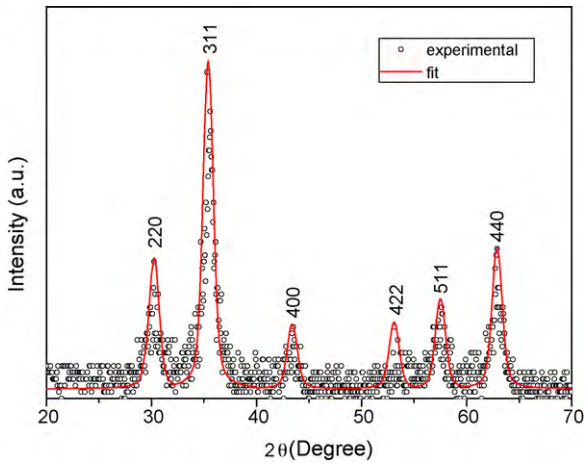

Fig. 1. XRD pattern and line profile fitting of HCIO nanoparticles.

3.2. FT-IR analysis

FT-IR spectra of iron oxide, L-histidine, HCIO nanoparticles and suggested linkage of L-histidine to iron oxide surface are given in Fig. 2(a)–(d). The presence of the iron oxide nanoparticles is evidenced by the strong absorbtion bands at around 570–590 cm^{-1} that confirm the metal-oxygen streching, present in Fig. 2(a) and (b) [17–20]. In the spectrum pure L-histidine (Fig. 2(c)) the characteristic NH_2 stretching frequencies of L-histidine is observed at ~3330 cm^{-1}, and asymmetric and symmetric stretching frequencies of carboxylate (COO^-) are observed at 1635 cm^{-1} $\nu_{as}(COO^-)$ and 1411 cm^{-1} $\nu_s(COO^-)$, respectively [18,21]. In the spectrum for HCIO (Fig. 2(c)), the vibrations of asymmetric and symmetric stretching of carboxyl anion occurred at 1607 and 1392 cm^{-1}. Also the peak at ~3400 cm^{-1} (Fig. 1(c)) is assigned to N–H stretching [22] in agreement with the vibrations of some aminocarboxylates and carboxylates reported earlier [23]. According to these results, FT-IR analyses suggest that L-histidine remains chemisorbed on the surface of iron oxide.

3.3. TGA analysis

Thermograms of iron oxide (Fe_3O_4), L-histidine and HCIO are presented in Fig. 3, which can be used for a quantitative com-

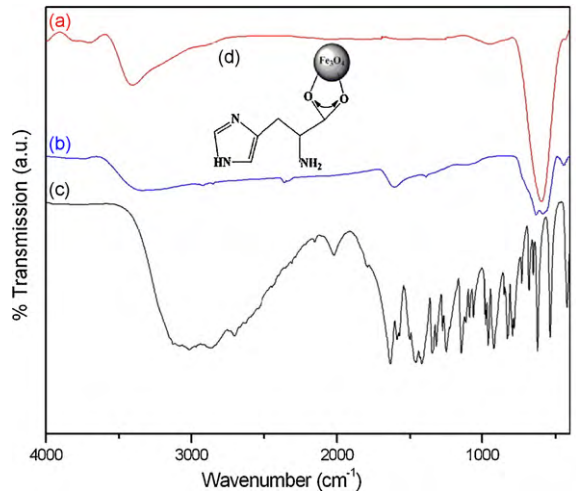

Fig. 2. FT-IR spectra of (a) iron oxide, (b) L-histidine and (c) HCIO nanoparticles (d) suggested linkage of L-histidine to iron oxide surface.

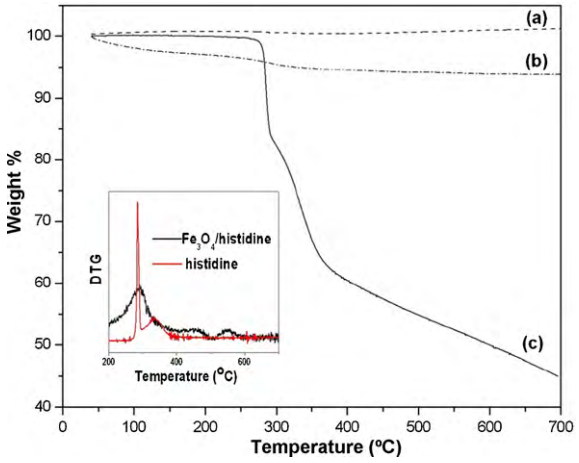

Fig. 3. TGA thermograms of (a) Fe_3O_4 NP's (b) HClO, and (c) L-histidine.

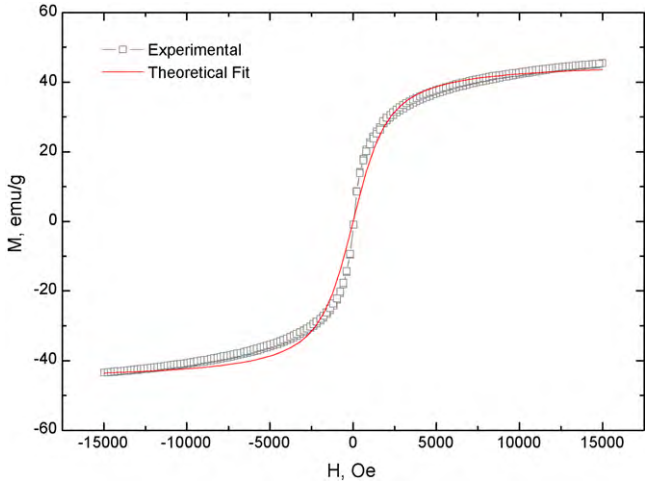

Fig. 5. Room temperature magnetization curve of HClO nanoparticles.

parison of degradation behavior of samples. Iron oxide shows no weight loss in the temperature range of TG analysis. On the other hand, the two-stage degradation is seen in the TGA curves of both L-histidine and HClO samples. L-Histidine also yields residue which indicates coke formation due to pyrolytic conditions under nitrogen. Unfortunately, the weight percent of this residue could not be determined due to the heating range of our TGA instrument. Derivative weight loss (DTG) curves of the L-histidine and HClO are also illustrated in the inset of Fig. 3 which shows a similar behavior in the degradation of these two samples. HClO sample shows a slight weight change up to 140–150 °C which is ascribed to the release of physiosorbed water, while L-histidine exhibits a considerable thermal stability up to 300 °C. Degradation of L-histidine over the iron oxide begins at a much lower temperature. This behavior could be originated from the fact that iron oxide particles behave as catalysts thus reducing the degradation temperature of L-histidine.

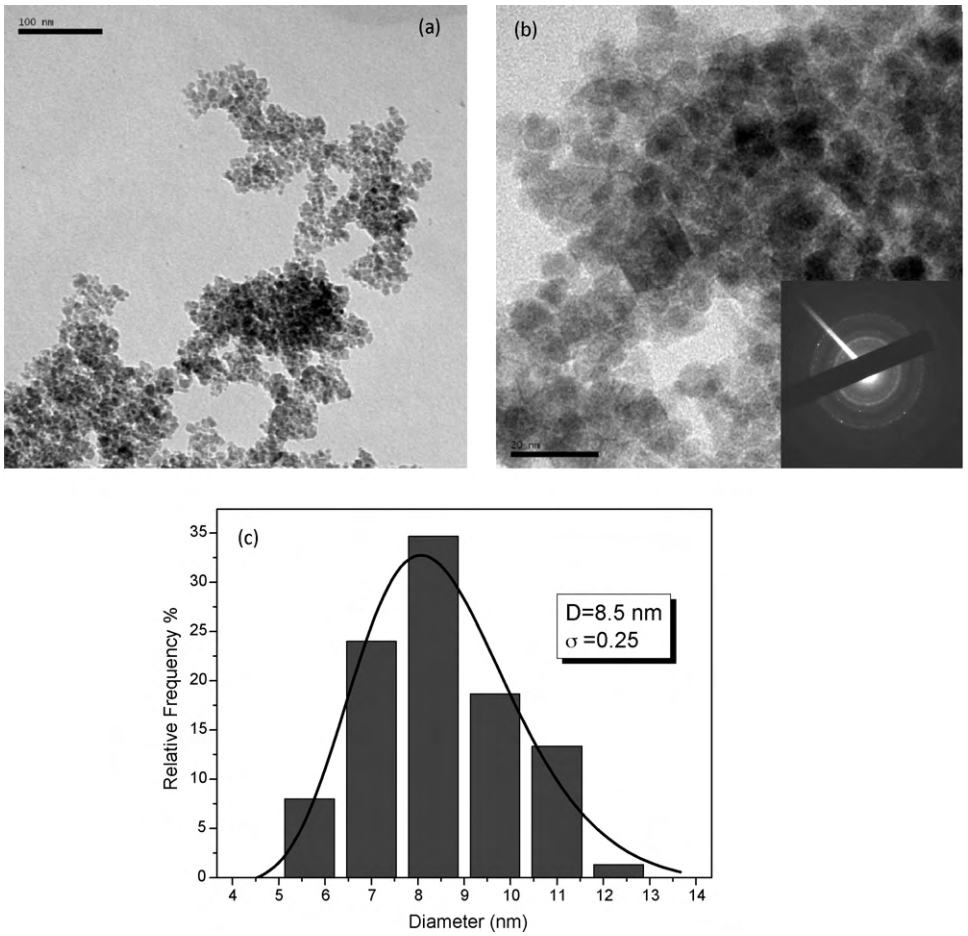

Fig. 4. (a and b) TEM micrographs of L-histidine-coated iron oxide (HClO) NP's at different magnifications, in the inset is shown the SAED pattern; (c) Calculated histogram from several TEM images with log-normal fitting.

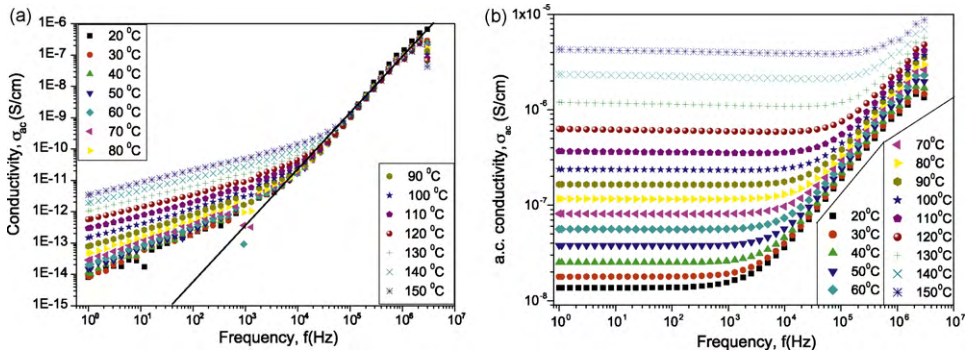

Fig. 6. *ac* conductivity of (a) L-histidine and (b) HCIO nanoparticles.

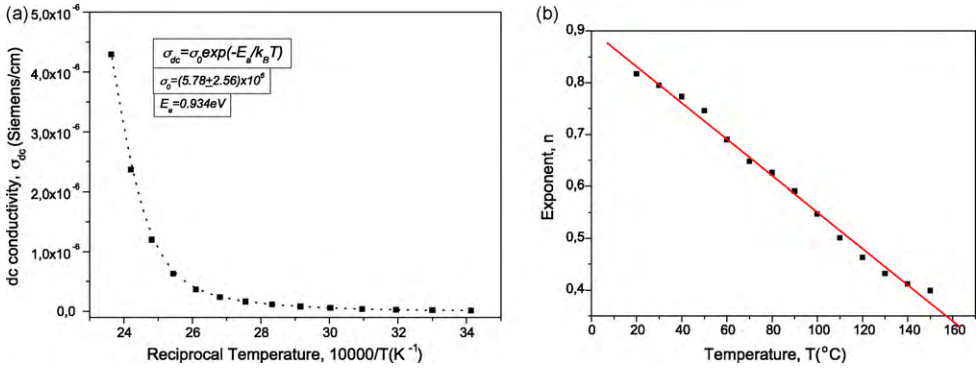

Fig. 7. (a) *dc* conductivity of HCIO nanoparticles (b) exponent *n* of L-histidine as a function of temperature for low frequencies.

3.4. TEM analysis

Morphology and size distribution of L-histidine coated iron oxide NPs was analyzed using TEM. Few micrographs at different magnifications and a histogram calculated thereof are presented in Fig. 4. Fe_3O_4 particles exhibit dominantly near spherical morphology. SAED pattern of HCIO is given in the inset of Fig. 4(b) which reveals crystalline nature of iron oxide nanoparticles. Average particle size calculated by log-normal fitting to the size distribution histogram, was obtained as 8.5 ± 0.25 nm. As compared with the crystallite size from X-ray line profile fitting, this reflects nearly single crystaline nature of the Fe_3O_4 nanoparticles.

3.5. Magnetization measurements

Fig. 5 shows the room temperature magnetization curve of the HCIO nanoparticles. The saturation magnetization is determined as 45.5 emu/g which is considerably lower than the theoretical M_s of the bulk magnetite (92 emu/g). This reduction is expected in NPs as the surface magnetic order can be affected by the structural distortions that can cause spin canting and existence of non-magnetic surface layer [24,25]. HCIO NPs do not saturate in an external field of 15 kOe. Moreover, there is no measurable coercivity and remanance. The weaker magnetization and lack of saturation have often been observed in iron oxide NPs [25,26]. All of these observations are characteristic features of superparamagnetic NPs having particle size smaller than 16 nm [27].

Magnetization of superparamagnetic particles can be described by the Langevin function which can be used to determine the particle size. Theoretical fitting to $M(H)$ curve in Fig. 5 gives the mean magnetic moment of the coated magnetite NPs as $5.616\mu_B$. Thus, using this value with the known M_s (45.5 emu/g), mean particle size is obtained as 7.6 ± 1.9 nm which agrees well with the values estimated from both TEM histogram and XRD line profile fitting.

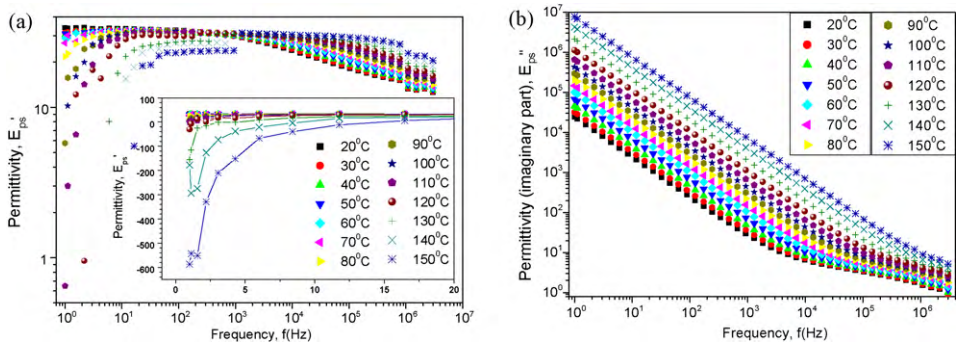

Fig. 8. (a) The real and (b) imaginary part of the permittivity of HCIO NPs.

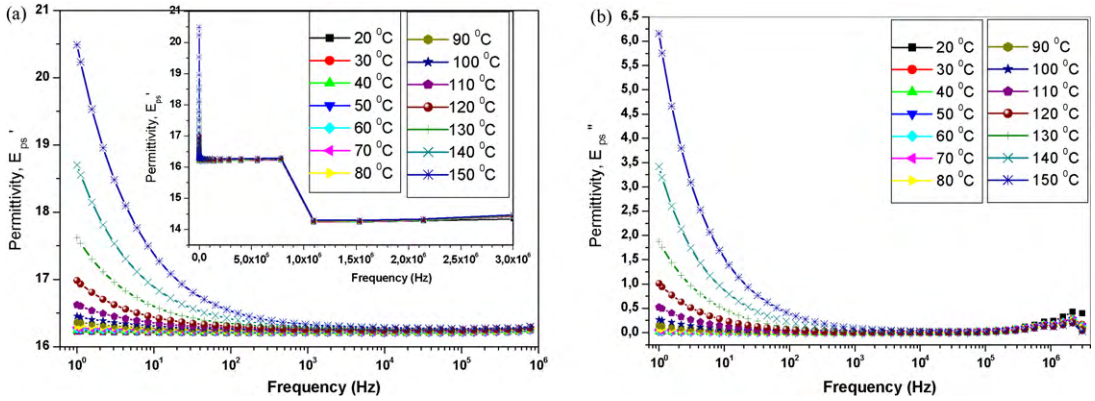

Fig. 9. (a) Real and (b) imaginary part of permittivity of L-histidine.

3.6. *dc–ac conductivity, and permittivity evaluation*

The *ac* conductivity, σ_{ac} (ω) of the HCIO nanoparticles has been measured from 20 up to 150 °C using impedance spectroscopy. Frequency-dependent *ac* conductivities, σ_{ac} (ω), have been obtained using the following standard equation [28,29];

$$\sigma'(\omega) = \sigma_{ac}(\omega) = \in''(\omega)\omega\varepsilon_0 \quad (1)$$

where $\sigma'(\omega)$ is the real part of conductivity, $\omega(=2\pi f)$ is the angular frequency of the signal applied to the samples, $\in''$ is the imaginary part of complex dielectric permittivity ($\in^*$) and $\varepsilon_0(=8.852 \times 10^{-14}$ F/cm) is the vacuum permittivity.

The *ac* conductivity of L-histidine for various temperatures is shown in Fig. 6(a). It is clear that the *ac* conductivity under a certain frequency, ~1 kHz for RT, 10 kHz for 150 °C, increases with temperature and is given with a frequency dependency of $\sigma_{ac}(\omega, T) = \sigma_0\omega^n$ for each of the relevant temperatures. Here exponent *"n"* is found to be linearly dependent on temperature for low frequencies of less than 10 kHz as $n(T) = a - sT$ where *a*, *s* are constants calculated from the curve of Fig. 6(b). However, at high frequencies *ac* conductivity varies with the same way but independent of temperature. In other word, *ac* conductivity over a frequency of 100 kHz obeys the rule of the temperature independent expression of $\sigma_{ac}(\omega) = \sigma_0\omega^n$ with an exponent *"n"* of about 2, where *n* is independent of temperature.

The *ac* conductivity of HCIO nanopaticles as a function of frequency at various temperatures is illustrated in Fig. 6(b). It is found from the *log–log* graph that, initially, the frequency independency of the conductivity at low frequency region exists. Then, after a certain frequency value, which is strongly temperature-dependent, it becomes a form of $\sigma_{ac}(\omega, T) = \sigma_0(T)\omega^n$ where the exponent *"n"* varies between 0.6 and 0.7 depending on the temperature.

The *dc* conductivity of HCIO nanoparticles is presented in Fig. 7(a). From the graph *dc* conductivity of the nanocomposites is found to obey the thermally activated conduction rule of $\sigma_{dc} = \sigma_0 \exp(E_a/k_BT)$ with activation energy of 0.934 eV. This represents the influence of the temperature on the conductivity of nanocomposites; a typical degree of the influence on conductivity of temperature.

When the frequency dependency of *ac* conductivity for both L-histidine and HCIO nanoparticles are compared with each other, it is clear that the conductivity at low frequencies is relevant to the nature of pure L-histidine structures like polymers [30]. However, L-histidine-capped-magnetite can modify the dependency of conductivity as a function of both temperature and frequency when compared with the pure one. As a result, because of the nature of both temperature and frequency dependency, the conductivity of HCIO NPs can be attributed to the ionic conductivity [31,32].

The real and imaginary parts of the complex permittivity of HCIO NPs are illustrated in Fig. 8(a) and (b), respectively. The real part of permittivity, which is related to the stored energy within the medium, is remained almost unchanged at low temperature while over a temperature of 130 °C is increased sharply up to a frequency of 15 Hz and saturated over it and again it happened as in the low temperature case (see the graph in the inset of Fig. 8(a)). The imaginary part of the permittivity, which is related to the dissipation (or loss) of energy within the medium, is found to be well-known attitude of the frequency dependency which can be expressed as $\varepsilon''(\omega) = \varepsilon''(0)\omega^{-n}$ where $\varepsilon''(0)$ is independent of frequency, but temperature-dependent up to 10 kHz (20 °C) to 1 MHz

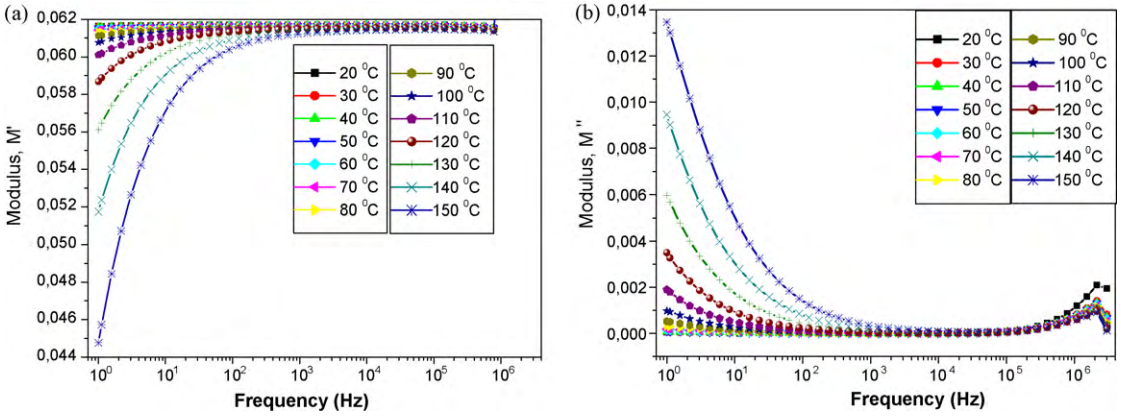

Fig. 10. (a) Real (b) imaginary part of modulus of pure L-histidine.

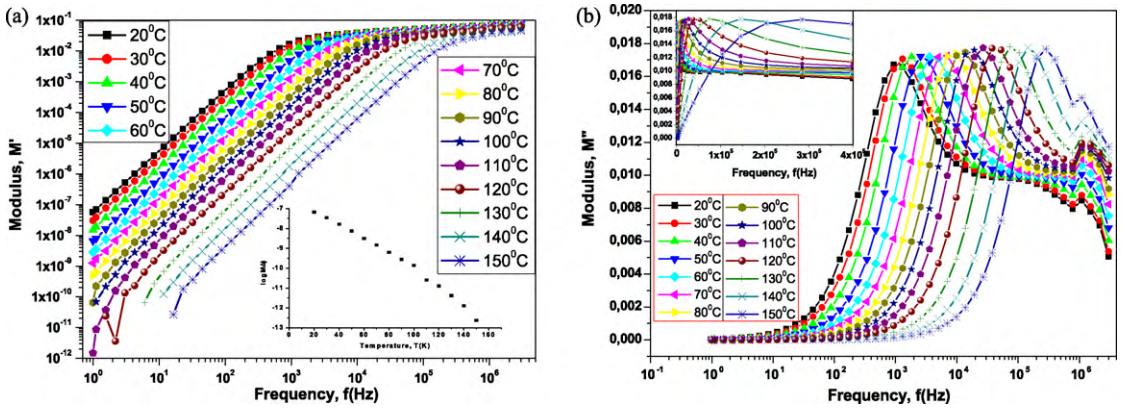

Fig. 11. (a) Real (b) imaginary part of modulus of HClO nanoparticles.

(150 °C), n is about unity for all temperatures studied here. At high frequency the imaginary part of permittivity becomes less sensitive to both frequency and temperature, tends to be stabilized as reported earlier [33]. These results for both real and imaginary part of the permittivity are attributed to the ionic relaxation process although dipolar contributions also exist at high frequency region [34,35].

The real and imaginary part of permittivity of L-histidine is shown in Fig. 9(a) and (b), respectively. Both components of the permittivity decreased exponentially and stabilized when reached around a frequency of 1 kHz and this stabilization continues up to 800 kHz, after that decreased sharply and stabilized again up to 3 MHz as depicted in the inset of Fig. 9(a).

Electric modulus formalism is a proper tool to study the polarization effect. The electric modulus can be calculated by the equation [36,37].

$$M^* = (\varepsilon^*)^{-1} = M' + iM'' = \frac{\varepsilon'}{\varepsilon'^2 + \varepsilon''^2} + i\frac{\varepsilon''}{\varepsilon'^2 + \varepsilon''^2} \quad (2)$$

Fig. 10 shows the electric modulus formalism of the pure L-histidine. As shown in Fig. 10(a), real parts of modulus (M') increase exponentially with frequency for various temperatures and reach a constant value and saturate as expected. The starting points of the curves depend strongly on the temperature. The imaginary part (M'') shows an exponential decrease with frequency and decay ratio varies with temperature as seen in Fig. 10(b). Additionally, at very low frequencies of less than 500 Hz, the real and imaginary parts of the modulus for all temperatures show that it increases and decreases sharply to a saturated values for all, respectively, but the starting values reduce/increase with temperature, respectively again, and than compensate the value at high frequencies for both. This type of relaxation processes is attributed to an interfacial polarization effects.

The real and imaginary parts of modulus of HClO nanoparticles are shown in Fig. 11(a) and (b). For all temperatures, the real part of modulus at lower frequencies obeys the rule of $M'(T, \omega) = M'_0(T)\omega^n$ where n (~2) varies from 1.9 to 2.1 depending on temperature. These tendencies continue up to 400 kHz for a temperature of 150 °C from 1 kHz for 20 °C. After that, the *log–log* graph shows that the frequency dependencies saturate and remain constant for all temperatures. Additionally, the temperature dependency of real component of the logarithmic *dc* modulus, $\log M'_0$, is found to vary almost linearly with temperature as illustrated in the inset of the Fig. 11(a). This can be attributed the temperature dependency of the polarization effect for an applied *dc* electric field.

In the imaginary part of the modulus, M'', the incremental threshold of the peak is shifted to higher frequencies as seen in the inset of the Fig. 11(b). So the peak at 20 °C is about 1 kHz while at 150 °C it is shifted and situated at about 400 kHz. This coincidence is correlated with real part of the modulus. This means that the frequency dependence of both parts of the modulus resembles to each other for the given temperature range. It is well known that the peak position in the imaginary part is strongly dependent to temperature. According to the electric modulus formalism of the pure L-histidine matrix, the temperature frequency of dielectric properties of the HClO nanoparticles can be explained as follows [38,39]. When the temperature is lowered, the expansion of pure L-histidine matrix will separate the filling components of the nanocomposites that connected with each other earlier. The interfaces between magnetites and L-histidine matrix will enhance, and the dielectric constant will rise. When the temperature is higher than a certain value, the L-histidine nanocrystallite phase begins to change, transforming from a semi-crystalline phase to the more disordered polymer-like region. The interfaces between the magnetites and the L-histidine matrix will decrease. So the dielectric constant will decrease. The polarization will be enhanced. In this case, the dielectric constant increases again. At higher frequency, the values of the electric modulus of both L-histidine and its magnetite composites become less temperature-dependent. As it is well known, solid polymer electrolytes have several advantages over the liquid counterpart such as desirable shape mouldability, mechanical strength and flexibility of design. Unfortunately, solid polymer electrolytes have the intuitive problem of low ionic conductivity at ambient temperature that acts as a barrier to their suitability. It can be understood that various physical and chemical factors such as crystallinity, synchronized cation-anion motions, and the formation of the ion-pair have a strong effect on ionic conductivity [40]. These factors reduce the cationic conductivity, and therefore this act as a barrier for potential applications.

In general, there are a few different mechanisms which influence the shape of the permittivity via frequency: Relaxation effects are associated with permanent and induced molecular dipoles. At low frequencies the applied electric field varies slowly enough to allow dipoles to reach equilibrium before the field has measurably changed. For higher frequencies at which dipole orientations cannot track the applied field due to the viscosity of the medium, so the absorption of the field energy results in energy dissipation. The mechanism of dipoles relaxing is termed as dielectric relaxation. Resonance effects originate from the rotations or vibrations of atoms, ions, or electrons. These processes are examined in the neighborhood of their characteristic absorption frequencies.

4. Conclusion

We have successfully synthesized L-histidine capped iron oxide nanoparticles in one pot process. The final product was analyzed

for composition, microstructure, *ac*–*dc* conductivity performance, and dielectric permittivity. L-Histidine is assessed to be covalently bonded to the iron oxide nanoparticle surface via carboxyl groups. Thermal analysis revealed that magnetic nanoparticles showed catalytic effect that caused an early degradation/decomposition of the L-histidine capping. Near spherical morphology was assessed by TEM and particle size calculated from TEM analysis and crystallite size calculated from XRD analysis reveal single crystalline nature of iron oxide NPs. Magnetic measurements reveal the superparamagnetic character of the nanocomposite. The *ac* conductivity showed a temperature independent behavior at low frequencies and temperature dependant behavior at high frequencies which is an indication of ionic conductivity. The *dc* conductivity of the nanocomposites is found to obey the Arrhenius plot with activation energy of 0.934 eV. The *ac* and *dc* conductivity measurements revealed semiconductor conduction characteristics, and various trends were observed, as a function of frequency and temperature, revealing different mechanisms dominating based on the temperature dependant reorganization of the nanocomposite. Permittivity measurements showed increasing dielectric constant with increasing temperature as expected from semiconductors. Analysis of electrical modulus and dielectric permittivity functions suggest that ionic and polymer segmental motions are strongly coupled in the nanocomposite.

Acknowledgements

The authors are thankful to the Fatih University, Research Project Foundation (Contract no: P50020902-2) and Turkish Ministry of Industry and Trade (Contract no: 00185.STZ.2007-2) for financial support of this study. MST acknowledges the fellowship from Knut and Alice Wallenbergs Foundation (No: UAW2004.0224).

References

[1] R.M. Cornell, U. Schwertmann, The Iron Oxides: Structure, Properties, Reactions, Occurrence and Uses, VCH, New York, 1996, pp. 28–29.
[2] J.M.D. Coey, A.E. Berkowitz, L.I. Balcells, F.F. Putris, F.T. Parker, Appl. Phys. Lett. 72 (1998) 734.
[3] S. Soeya, J. Hayakawa, H. Takahashi, K. Ito, C. Yamamoto, A. Kida, H. Asano, M. Matsui, Appl. Phys. Lett. 80 (2002) 823.
[4] V.P. Torchilin, Eur. J. Pharm. Sci. 11 (2000) S81.
[5] L. Juillerat-Jeanneret, F. Schmitt, Res. Rev. 27 (2007) 574.
[6] G. Hongwei, X. Keming, Y. Zhimou, C.K. Chang, B. Xu, Chem. Commun. 34 (2005) 4270.
[7] C.V. Mura, M.I. Becker, A. Orellana, D. Wolff, J. Immunol. Methods 260 (2002) 263.
[8] G. Marinescu, L. Patron, D.C. Culita, C. Neagoe, C.I. Lepadatu, I. Balint, L. Bessais, C.B. Cizmas, J. Nanopart. Res. 8 (2006) 1045.
[9] S.L. Tie, Y.Q. Lin, H.C. Lee, Y.S. Bae, C.H. Lee, Colloid Surf. A Physicochem. Eng. Aspects 273 (2006) 75.
[10] Jong Kuk Lim, Youngmin Kim, So Yeong Lee, Sang-Woo Joo, Spectrochimica Acta Part A 69 (2008) 286.
[11] T. Ishikawa, S. Kataoka, K. Kandori, J. Mater. Sci. 28 (1993) 2693.
[12] C.D. Culita, M. Gabriela, L. Patron, O. Carp, C.B. Cizmas, L. Diamandescu, Mater. Chem. Phys. 111 (2008) 381.
[13] M.S. Toprak, B.J. McKenna, M. Mikhaylova, J.H. Waite, G.D. Stucky, Adv. Mater. 19 (2007) 1362.
[14] M.H. Sousa, J.C. Rubim, P.G. Sobrinho, F.A. Tourinho, J. Magn. Magn. Mater. 67 (2001) 225.
[15] T. Wejrzanowski, R. Pielaszek, A. Opalińska, H. Matysiak, W. Lojkowski, K.J. Kurzydlowski, Appl. Surf. Sci. 253 (2006) 204.
[16] R. Pielaszek, Analytical expression for diffraction line profile for polydispersive powders, in: Appl. Crystallography, Proceedings of the XIX Conference, Krakow, Poland, 2003, p. 43.
[17] L.J. Kirwan, P.D. Fawell, W.V. Bronswijk, Langmuir 19 (2003) 5802.
[18] Z. Durmus, H. Kavas, M.S. Toprak, A. Baykal, T.G. Altınçekiç, A. Aslan, A. Bozkurt, S. Coşgun, J. Alloys Compd. 484 (2009) 371.
[19] M. Mikhaylova, D.K. Kim, C.C. Berry, A. Zagorodni, M. Toprak, A.S.G. Curtis, M. Muhammed, Chem. Mater. 16 (2004) 2344.
[20] T Özkaya, M.S. Toprak, A. Baykal, H. Kavas, Y. Köseoğlu, B. Aktaş, J. Alloys Compd. 472 (2009) 18–23.
[21] A.M. Petrosyan, Vibrat. Spectrosc. 43 (2007) 284.
[22] J.Y. Park, E.S. Choi, M.J. Baek, G.H. Lee, Mater. Lett. 63 (2009) 379.
[23] J.A. Kieft, K. Nakamoto, J. Inorg. Nucl. Chem. 29 (1967) 2561.
[24] P. Morales, S. Veintemillas-Verdaguer, M.I. Montero, C.J. Serna, A. Roig, L. Casas, B. Martinez, F. Sandiumenge, Chem. Mater. 11 (1999) 3058.
[25] N. Kemikli, H. Kavas, S. Kazan, A. Baykal, R. Ozturk, J. Alloys Compd., doi:10.1016/j.jallcom.2010.04.192.
[26] K. Uzun, E. Çevik, M. Şenel, H. Sözeri, A. Baykal, M.F. Abasıyanık, M.S. Toprak, J. Nanopart. Res., doi:10.1007/s11051-010-9902-9.
[27] J. Mürbe, A. Rechtenbach, T. Töpfer, Mater. Chem. Phys. 110 (2008) 426.
[28] B. Unal, Z. Durmus, H. Kavas, A. Baykal, M.S. Toprak, Mater. Phys. Chem. 123 (2010) 184.
[29] S.U. Celik, A. Bozkurt, Eur. Polym. J. 44 (2008) 213.
[30] B. Unal, M.S. Toprak, Z. Durmus, H. Sözeri, A. Baykal, J. Nanopart. Res., doi:10.1007/s11051-010-9898-1.
[31] A. Baykal, N. Bıtrak, B. Unal, H. Kavas, Z. Durmus, S. Ozden, M.S. Toprak, J. Alloys Compd. 502 (2010) 199.
[32] H. Kavas, Z. Durmus, A. Baykal, A. Aslan, A. Bozkurt, M.S. Toprak, J. Non-Cryst. Solids 356 (2010) 484.
[33] Y. Köseoğlu, M. Bay, M. Tan, A. Baykal, H. Sözeri, R. Topkaya, N. Akdoğan, J. Nanopart. Res., doi:10.1007/s11051-010r-r9982-6.
[34] D.J. Griffiths, Introduction to Electrodynamics, 3rd ed., Prentice Hall, 1998, ISBN 0-13-805326-X.
[35] J.D. Jackson, Classical Electrodynamics, 3rd ed., Wiley, New York, 1999, ISBN 0-471-30932-X., Secti 7.5.B, and 7.5C.
[36] G.M. Tsangaris, O.C. Psarras, N. Kouloumbi, J. Mater. Sci. 33 (1998) 2027.
[37] S. Abdul-lawad, A. Alnajjar, M.H. Abdallah, Appl. Phys. A: Mater. Sci. Process. 64 (1997) 199.
[38] S. Yu, P. Hing, X. Hu, J. Appl. Phys. 88 (2000) 398.
[39] V. Bobnar, A. Levstik, C. Huang, Q.M. Zhang, J. Non-Cryst. Solids 353 (2007) 205.
[40] D.K. Pradhan, R.N.P. Choudhary, B.K. Samantaray, Int. J. Electrochem. Sci. 3 (2008) 597.